JOURNAL OF THERMOPHYSICS AND HEAT TRANSFER
Vol. 12, No. 2, April–June 1998

Spectroscopic Emission Measurements Within the Blunt-Body Shock Layer in an Arcjet Flow

Chung S. Park,* Mark E. Newfield,† Douglas G. Fletcher,‡ Tahir Gökçen,† and Surendra P. Sharma§
NASA Ames Research Center, Moffett Field, California 94035-1000

In the present study, radiation emanating from the freestream and shock-layer flow over a 15.24-cm-diam, flat-faced cylinder model was measured in the NASA Ames Research Center's 20-MW Arcjet Facility. The test gas was a mixture of argon and air. Spatially resolved emission spectra were obtained over a 200- to 890-nm wavelength range using a charged-coupled device camera (1024 × 256 array) attached to a spectrograph. The optical system was calibrated using tungsten and deuterium radiation sources. Analytical tools were used to determine the following line-of-sight-averaged thermodynamic properties from the calibrated spectra: 1) rotational temperature of the freestream and 2) rotational, vibrational, electronic temperatures, and species number densities within the shock layer. An analysis was performed to estimate the uncertainty bounds of the determined properties.

Nomenclature

C = constant
I = atomic line intensity, W/cm^3
L = optical path length, cm
m = magnification
n = number density, cm^{-3}
P = peak value of a band system, W/cm^2 μm − sr
T = temperature, K
W = area under a spectra, W/cm^2 sr
x = distance from the model surface, mm
θ = characteristic temperature, K
σ = standard deviation

Subscripts
e = electronic
r = rotational
v = vibrational

Introduction

ARCJET wind-tunnel facilities produce high-enthalpy hypersonic flows that have been used for purposes as diverse as testing spacecraft thermal protection materials, investigating catalytic recombination of atoms on surfaces, and simulating combustion in airbreathing engines operating at hypersonic speeds. Despite this broad utility, arcjet flows are not well understood. The present study is aimed at improving our knowledge of these flows through the acquisition and analysis of radiative emission from the freestream and shock-layer flow over a blunt-body test article. These measurements are part of an ongoing effort to fully instrument and diagnose the flow in the NASA Ames Research Center's 20-MW Aerodynamic Heating Facility (AHF) using optical instrumentation.

Although the spectral emission measurement approach is conceptually simple, the interpretation of radiation from arcjet flows can be quite difficult because of nonequilibrium thermochemical effects. In the operational conditions of AHF, thermochemical relaxation processes of the expanding nozzle flow are slowed because of low gas pressure, and freezing phenomena often occur in the nozzle.[1] Thus, the freestream is typically in both thermal and chemical nonequilibrium.

In previous experimental studies, efforts have been made to characterize the thermochemical state of the freestream and shock-layer flow in arcjet facilities.[2,3] One particular experiment sought to determine the flow enthalpy by analyzing the radiative emission from a blunt-body shock layer.[4] Therein, the enthalpy of the flow was deduced based on the act that spectral features of radiation are a function only of pressure and enthalpy at equilibrium, assuming equilibrium conditions were achieved in the shock-layer flow.

In the present work, tests were conducted at conditions more likely to generate a region of thermochemical equilibrium within the shock layer, i.e., at higher stagnation pressure and with a large diameter test model. Several methodologies were used to extract useful information from time-averaged emission spectra of the freestream and the blunt-body shock layer that were spatially resolved along the stagnation streamline.[5] The obtained information includes 1) T_r of the freestream using the NO γ and δ systems; and 2) T_r, T_v, and T_e of the shock layer using the N_2^+ 1− system and atomic oxygen lines. Based on the measured temperatures, the line-of-sight (LOS)-averaged number densities of N_2^+, N_2, and CN were determined from the shock-layer emission spectra. Uncertainty analyses of the measured temperatures and number densities were performed to estimate possible errors in the determined values. As part of this analysis, the light acceptance cone shaped by the optical arrangements of the experimental setup was studied using ray-tracing software.

Experiment

Apparatus

The experiments were conducted in the 20-MW AHF at NASA Ames Research Center. A schematic of the facility and experimental setup is shown in Fig. 1. The test gas was heated in a 216-cm-long, 6-cm-diam constrictor section. The constrictor was followed by a 10-cm-long, 10.4-cm-diam settling chamber. Downstream from the settling chamber, the flow was expanded through a converging–diverging conical nozzle. The nozzle had a throat diameter of 3.81 cm and exit diameter of 30.48 cm. The conical converging sections had half-angles of 22 and 45 deg, and the diverging section had a half-angle of

Presented as Paper 97-0990 at the AIAA 35th Aerospace Sciences Meeting, Reno, NV, Jan. 6–9, 1997; received March 10, 1997; accepted for publication Oct. 27, 1997.

*Senior Research Scientist, Thermosciences Institute, Reacting Flow Environments Branch. Member AIAA.
†Research Scientist, Reacting Flow Environments Branch.
‡Research Scientist, Reacting Flow Environments Branch. Member AIAA.
§Senior Researcher, Reacting Flow Environments Branch. Associate Fellow AIAA.

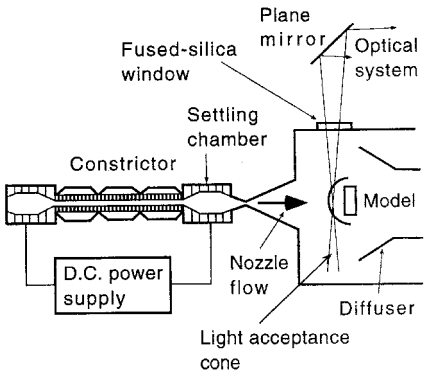

Fig. 1 Schematic of the facility and experimental setup.

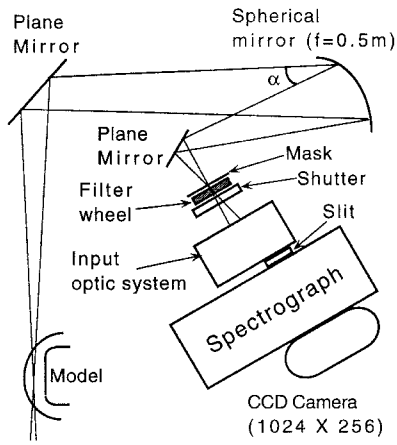

Fig. 2 Arrangement of m = 0.25 optical system.

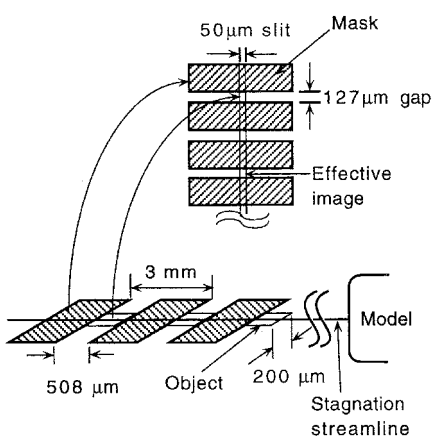

Fig. 3 Object and the image determined by the m = 0.25 optical system in Fig. 2.

8 deg. A 15.24-cm-diam, water-cooled copper model was used to generate the shock-layer flow.

As shown in Fig. 2, mirrors in the optical train were arranged such that radiation emanating from a 2.5-cm section along the stagnation streamline upstream of the model was imaged with a magnification m of 0.25 onto a mask with eight distinct rectangular apertures (Fig. 3). The radiation was then reimaged at m = 1 along the entrance slit of a 27.5-cm focal length spectrograph.

The spectrograph entrance slit width was set at 50 μm, and the f number of the optical system was 50. The limiting aperture was a 5-cm-diam mask mounted on a 50-cm focal length spherical mirror. An m = 1 input optics system was installed to correct astigmatism from the spherical mirrors of the spectrograph and provide a flat image field at the exit plane. Figure 3 shows the orientation of the rectangular apertures in the mask. Ignoring the aberrations and considering only one rectangular aperture in the mask, the m = 0.25 imaging optics, and the 50-μm entrance slit width, radiation emanating from an object area of 200 × 508 μm was imaged to a size of 50 × 127 μm, and subsequently reimaged at m = 1 onto the spectrograph entrance slit. With the mask segmented into eight distinct apertures, radiation was collected from eight object area locations along the stagnation streamline, with each location separated by approximately 3 mm.

The spectrograph was operated with a 1200-g/mm, 300-nm blaze ruled grating and an entrance slit width of 50-μm. The reciprocal linear dispersion of the system was 3 nm/mm. Time-averaged emission spectra were captured by a 1024 × 256 charged-coupled device (CCD) camera array mounted at the 25-mm-wide exit plane of the spectrograph and oriented such that the 1024 pixel side represented wavelength, while the 256 pixel side coincided with the direction of the stagnation streamline. With a 27-μm square pixel, the coverage of the array was limited to approximately 80 nm in wavelength and 25 mm of imaging along the stagnation streamline for the m = 0.25 optical system. The spectral resolution on the array and instrumental broadening were determined to be 0.08-nm/pixel and 0.16-nm full-width at half-maximum (FWHM), respectively.

During a single arcjet test, emission spectra were obtained at several different grating positions as shown in Table 1. The filter wheel, shutter, spectrograph grating, and CCD camera were all remotely operated by a personal computer. The filters and shutter integration times indicated for each wavelength region were chosen to minimize stray light, remove higher-order spectra, and prevent the CCD camera array from saturating. Three model test configurations were implemented in the experiment. Freestream radiation was recorded with the model translated out of the flow. Emission spectra within the blunt-body shock layer were captured with the model located 34.5 cm downstream from the nozzle exit. A separate test was performed at the same test conditions with the model moved an additional 2.4 cm downstream from the nozzle exit to capture spectra in close proximity to the bow shock.

Test Conditions

The arc heater was operated with a settling chamber pressure of 6.88 × 10^5 Pa, stagnation pressure on the model of 1.11 × 10^4 Pa, an arc current of 2075 A, and a voltage of 5630 V. The test gas was estimated to consist of 95% air and 5% argon by mass.

Calibration of Optical System

The measured emission spectra were corrected for the spectral response of the mirrors, filters, grating, and CCD array, and placed on an absolute intensity scale. Two National Institute of Standards and Technology (NIST) traceable standards of spectral radiance, a deuterium lamp (Optronics UV-401R)

Table 1 Useful wavelength range, test configuration, filter and shutter exposure time t for each grating position l [a]

λ, nm	Range, nm	Test configuration	Filter	τ, s
240	200–280	Freestream	None	30
240	200–280	Stray light	WG-320	30
240	200–280	Shock layer	None	0.1
300	260–340	Shock layer	None	0.1
330	290–370	Shock layer	BG-28	1.2
370	340–400	Calibration	WG-320	0.1
426	386–466	Shock layer	BG-28	0.5
460	420–500	Shock layer	BG-28	1.5
760	720–800	Shock layer	O.D. = 1	0.2
850	810–890	Shock layer	O.D. = 1	0.2

[a]O.D. represents the optical density of the neutral density filter.

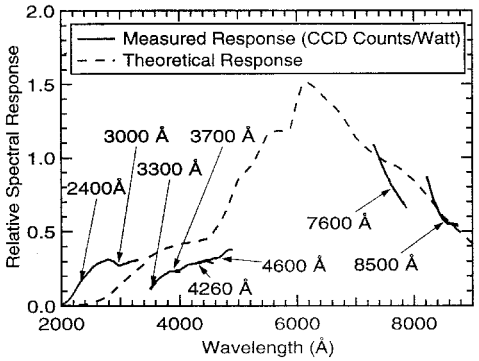

Fig. 4 Relative spectral response of the detection system.

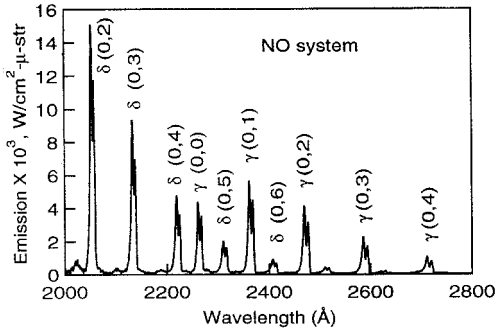

Fig. 5 Freestream spectra taken at 34.5 cm from the nozzle exit.

and a tungsten ribbon-filament lamp (GE 30A/T24/13), were used to calibrate the optical system. For the deuterium lamp, the uncertainty in spectral radiance values was specified by the calibration laboratory as ±10% below 250 nm and ±5% from 250 to 400 nm; for the tungsten lamp, uncertainty was specified to be no greater than ±4.5% from 225 to 890 nm. In the current section, the uncertainty represents the error bound of peak-to-peak value, which means that the odds are 1-to-1.

Both lamps were required for calibration of the optical train over the 200–890 nm range of interest in the experiment. The deuterium lamp coverd the spectral range from 200 to 400 nm; the tungsten lamp was used from 350 to 890 nm. The overlapping region for both lamp calibrations was therefore limited to the 350–400 nm spectral region. Within this wavelength range, the agreement between the two calibrations was ±4%, which is within the specified uncertainties in spectral radiance values. However, the overall uncertainty in absolute intensity when the calibration was applied in the experiment was estimated to be approximately ±16% below 250 nm and ±7% above 250 nm.

Figure 4 shows the measured spectral response of the entire detection system for the eight spectrograph grating positions used in the experiment. Therein, the measured spectral response curves were generated considering the corrections for filter transmission characteristics at each grating position. The measured response was normalized to compare with a theoretical system response curve, which is also shown in Fig. 4. The normalized theoretical response was derived from the ideal relative spectral response of the individual system components. This calculation includes the reflectivity of 11 mirror surfaces, the grating efficiency, and the radiant sensitivity of the unintensified CCD array. Because idealized spectral response quantities were used for the theoretical curve, it is not surprising that there is only qualitative agreement between the theoretical and measured distributions.

Measured Spectra

Freestream

Emission spectra from the freestream were recorded with the model translated out of the flow. The emission spectra were taken at the wavelength intervals in Table 1 and the only significant radiation emanated from NO in electronically excited states, as shown in Fig. 5. The spectrum in Fig. 5 is one of the eight spectra taken simultaneously by the CCD camera. The other seven spectra were identical to that in Fig. 5.

As indicated in Fig. 5, the spectral bands detected were identified as the NO γ and δ systems. For both systems, only vibrational transitions from the upper level of $v' = 0$ were of sufficient intensity to be recorded during the exposure time. Emission from higher vibrational levels was not discernible above the background light level, which is clearly evident between the designated spectral features in Fig. 5.

To measure the contribution of stray light from longer wavelengths to this background signal, a long pass filter (WG-320) was used, as indicated in Table 1. This measurement showed that the light level from longer wavelengths was less than 2% of the peak value of the signal, which implied the existence of unidentified band systems in the background signal. In the current analysis, however, no further effort was made to identify the background because the background signal did not show any significant features.

Shock Layer

A complete image of the shock-layer flow was obtained by positioning the water-cooled copper model at two locations: 34.5 and 36.9 cm downstream from the nozzle exit and recording complete sets of spectral data for each location. At each location of the model, eight spectra were recorded simultaneously for each grating position of the spectrograph. In Fig. 6, only 14 spectra of the two sets of eight spectra are shown for a single grating position. The wavelength range for this setting is 3860–4660 Å, and alongside the spectra, the x value represents the distance from the model surface. For x greater than 33.17 mm, the signal levels became very weak. This implies that these locations were outside of the shock layer; consequently, spectra from these locations were not considered in the following study.

In Fig. 7, emission spectra taken at the wavelength intervals in Table 1, at a location 17.90 mm from the model surface, are shown. (To reduce the number of figures, some spectra are merged into longer regions.) In the 2000- to 3000-Å wavelength range, as shown in Fig. 7a, NO γ was the most significant system. The other electronic transitions of NO were also most likely contributing to the spectra.

In the 3050–3650 and 3950–4820 Å range, as shown in Figs. 7b and 7c, the identified transitions were attributed to NO γ, N_2 2+, N_2^+ 1−, and CN violet systems. Also, several Cu atomic lines were identified. This was expected because copper was present in the stream as a contaminant resulting from electrode surface erosion. One of the purposes for taking spectra in this range was to detect the existence of OH molecules from dissociated water vapor that may enter the stream from leaks in heater cooling passages. For these tests, no OH spectra were detected. As indicated in Table 1, a BG-28 filter was used to remove: 1) the higher-order spectra from the short wavelength range and 2) the stray light from the longer wavelength range.

Example spectra for the 7300–8800 Å range are shown in Fig. 7d. The dominant emission features are O and N atomic lines, with a broad background contribution from N_2 1+ system emission. As seen in Fig. 7d, the O-atom emission was substantially stronger than that from N atoms. A neutral density filter and short exposure times at these grating positions (see Table 1) were chosen to keep the O-atom emission from saturating the detector. At spatial locations closer to the model surface, which are not shown, the N-atom emission level was not much greater than the N_2 1+ emission that underlies it. This made it impractical to attempt to extract information from the N-atom emission, despite the large number of recorded multiplet signals.

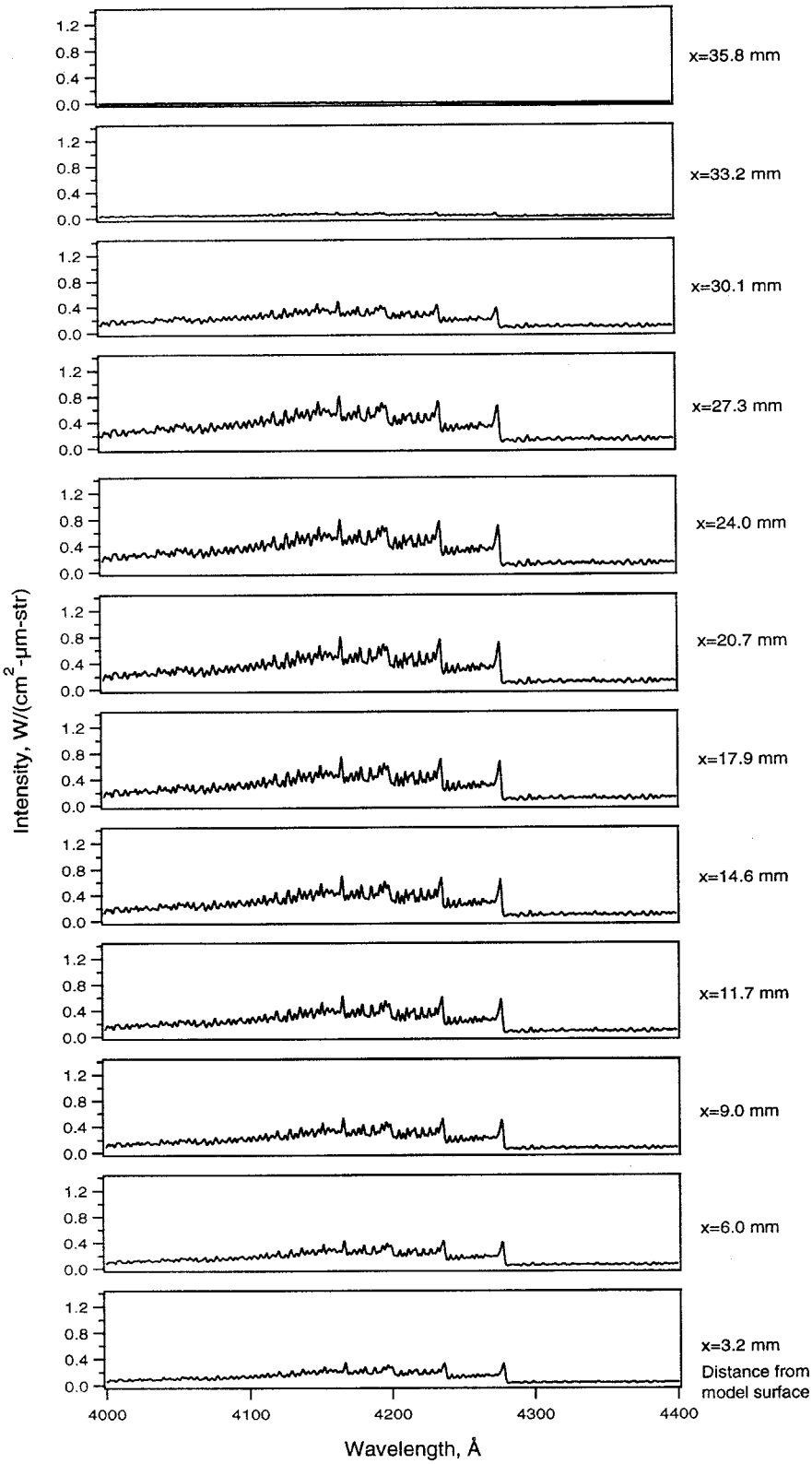

Fig. 6 Spectra of the shock layer of a model located 36.9 cm downstream of the nozzle exit. *X* represents the distance from the model surface in mm.

Data Analysis and Results

LOS-averaged values of rotational, vibrational, electronic temperature, and species number densities were determined from the measured emission spectra using the methodologies in Ref. 5. Uncertainties for each determined quantity were also calculated and presented with the odds of 2 to 1 in this section.

Freestream

The rotational temperature T_r was determined from the well-resolved vibrational bands in Fig. 5. The FWHM of the band intensity was calculated for a range of conditions and correlated with T_r. In Fig. 8, the FWHM of the NO $\gamma(0, 1)$ band is plotted as a function of T_r at a fixed instrumental line width

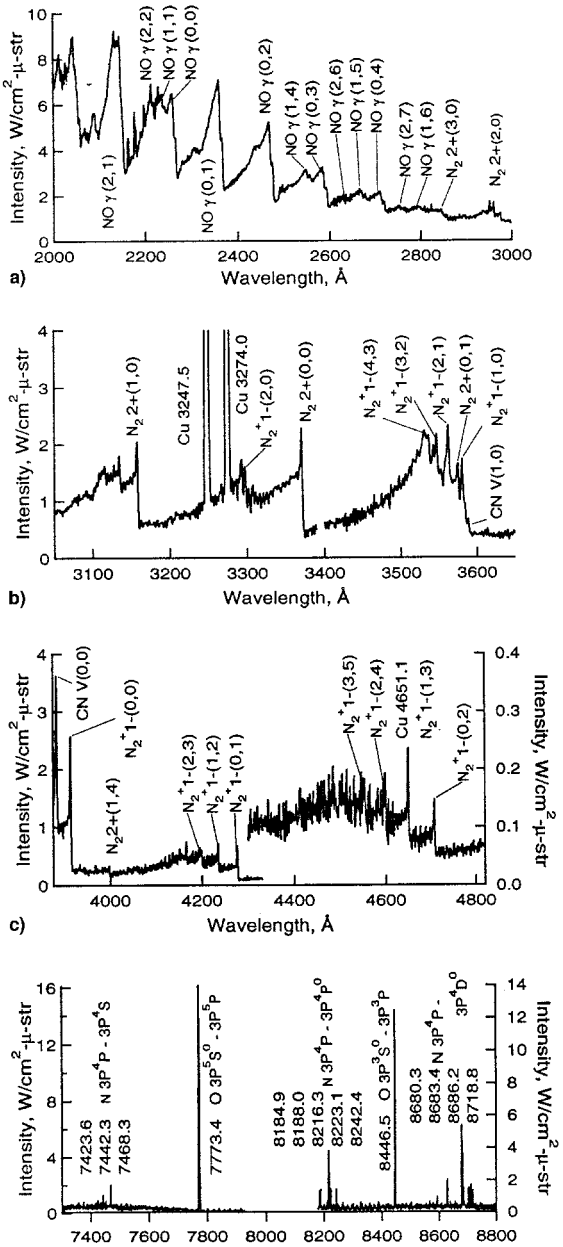

Fig. 7 a) Spectra of shock layer around a flat-faced cylindrical model of 15.24 cm in diameter. The spectra was taken at 17.90 mm away from the model surface. b)–d) Shock-layer emission spectra at the same condition of Fig. 6.

of 0.16 nm. Therein, the correlation between T_r and the FHWM was generated using the NEQAIR code.[6] NEQAIR generates synthetic spectra by calculating all of the atomic lines and molecular band systems line-by-line and then summing contributions at each wavelength. In the current study, a new version of NEQAIR with modifications suggested in Ref. 7 was used. For each measured FWHM of the NO $\gamma(0, 1)$ band from the spectra in Fig. 5, a T_r value was obtained using the correlation.

As mentioned, there was an unidentified background signal in Fig. 5. Even though the magnitude of the background signal relative to the identified NO band system was small in the wavelength range below 215 nm, the error in temperature because of this background signal was significant. Also, the vibrational bands with small Franck–Condon factors had lower signal-to-noise ratios. Thus, in the current study, only five bands were used to determine T_r: NO $\delta(0, 4)$, $\gamma(0, 0)$, $\gamma(0, 1)$, $\gamma(0, 2)$, and $\gamma(0, 3)$. The temperature determined from these bands are listed in Table 2, along with the uncertainties for each determination.

Table 2 Determined T_r for each band system of NO[a]

Parameter	$\delta(0, 4)$	$\gamma(0, 0)$	$\gamma(0, 1)$	$\gamma(0, 2)$	$\gamma(0, 3)$
T_R	875	856	938	930	942
σ_1	13	35	25	28	21
σ_2	22	34	27	16	13
σ_t	36	48	38	32	24

[a] σ_1 and σ_2 represent the errors because of the background signal and random errors, respectively. σ_t is the combination of σ_1 and σ_2. The values are in units of K.

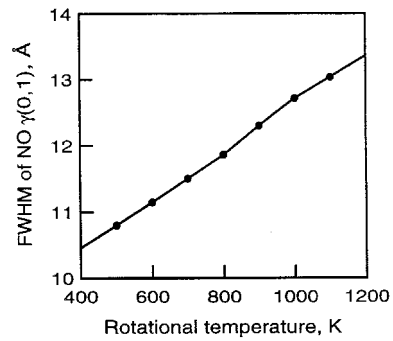

Fig. 8 FWHM of NO $g(0, 1)$ band system as a function of rotational temperature.

As evident in Fig. 5, the background signal directly affected the maximum value of each band system. Based on the T_r value in Table 2 (and $T_v \geq 950$ K), a synthetic spectrum was generated. The difference between the synthetic spectrum and experimental data, after adjusting the synthetic peak value to match the experiment, was taken as the unresolved background signal. The standard deviation of this background signal level adjacent to each band system was calculated and then used as an estimate of the uncertainty in the maximum value of the band system signal. The error in T_r, σ_1, was estimated using the relation[8]

$$\sigma_1 = \sqrt{\left(\frac{\partial T_r}{\partial P}\,\delta P\right)^2} \tag{1}$$

where P is the peak or maximum of each band system. The values of σ_1 are listed in Table 2.

For each band system, T_r was determined from eight spectral measurements and the values did not show any systematic trend. Thus, the measurements could be considered as eight independent measurements rather than a single sample measurement at eight locations. The standard deviation of the eight T_r values determined from each band system is listed as σ_2 in Table 2. The standard deviation of the combination of the two independent errors σ_t was calculated using the relation[8]

$$\sigma_t = \sqrt{\sigma_1^2 + \sigma_2^2}$$

and is also listed in Table 2. As seen in Table 2, the determined T_r value from each band system was within the estimated error bound of T_r from the other band systems.

Shock Layer

Temperature

As detailed in Ref. 5, integrals over wavelength in certain regions of the spectra were used to determine T_r. In Fig. 9, the intervals in the (0, 0) band system are shown by the extent of the shaded regions and these represent the actual integrated areas used in the analysis. As indicated in Fig. 9, the area baseline was taken from the minimum near the bandhead

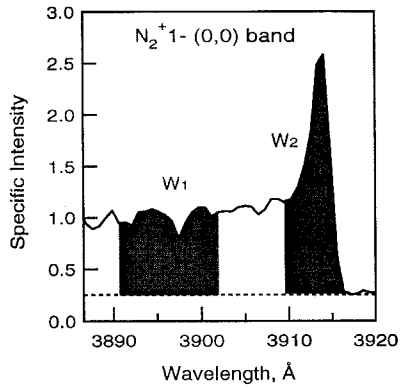

Fig. 9 Pair of areas that represent the integrated specific intensity used in the determination of rotational temperature.

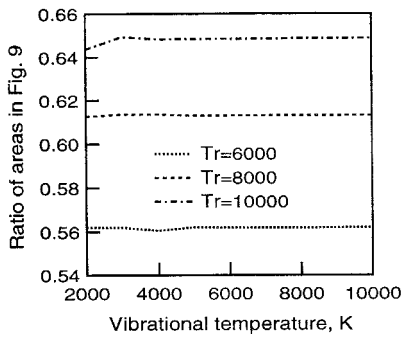

Fig. 10 Ratio of the areas in Fig. 9 as a function of vibrational temperature.

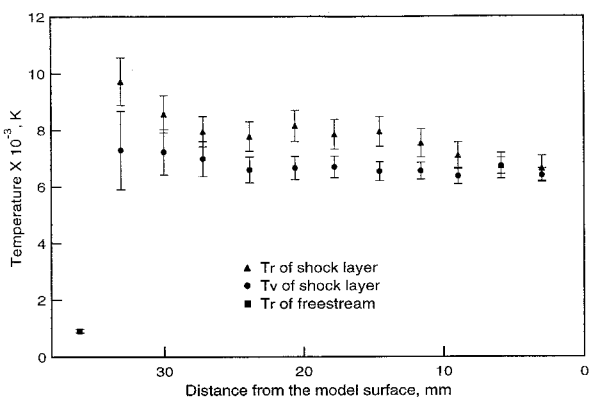

Fig. 11 Rotational and vibrational temperatures as functions of the distance from the model surface.

rather than the absolute zero of the spectral intensity to reduce the contribution of any unresolved background light to the integrals.

As was the case for the freestream, the area ratio was correlated with T_r over a range of temperatures using NEQAIR. In Fig. 10, the correlation between the area ratio in Fig. 9 and T_r is plotted. Curves, which represent the area ratio as a function of vibrational temperature, are shown for three different rotational temperatures. Clearly, this area ratio is a very weak function of T_v, which indicates that the areas identified in Fig. 9 should be a reliable indicator of T_r.

The ratios obtained from the measured spectra used to determine the T_r based on the correlation in Fig. 10. The values of T_r were determined for each axial position along the stagnation streamline for the shock-layer flow over the test model and plotted in Fig. 11.

The uncertainty in T_r was mainly because of the background signal that is thought to consist of stray light and contributions from unidentified species. As was done for the freestream data evaluation, a synthetic background spectrum was generated by using the determined temperatures in Fig. 11 to generate an emission spectrum with NEQAIR, which was then subtracted from the measured spectrum after adjusting the peak heights to match. The integration of this synthetic background spectra over the fixed wavelength bandwidths in Fig. 9 was calculated as a function of wavelength. The standard deviation of the integrated background signal was then taken as representative of the uncertainty in the areas. Based on the analysis in Ref. 8, the standard deviation of T_r, σ_{T_r}, was calculated as

$$\sigma_{T_r} = \sqrt{\left(\frac{\partial T_r}{\partial W_1}\sigma_{W_1}\right)^2 + \left(\frac{\partial T_r}{\partial W_2}\sigma_{W_2}\right)^2} \tag{2}$$

where W_1 and W_2 represent the shaded areas in Fig. 9, and σ_{W_1} (or σ_{W_2}) represents the standard deviation of W_1 (or W_2) caused by the background signal. The estimated σ_{T_r} is plotted in Fig. 11 as an error bar. Because ratios of spectral features from a single vibrational band were used to determine the rotational temperatures, it is expected that uncertainties in the calibration of the spectral intensities and uncertainties in relative transition strength factors will be negligible in comparison to the contribution from the unresolved background signal.

To determine T_v from N_2^+ 1− system emission, similar approaches to those used in T_r evaluation were used. Intervals for area ratios were taken from two band systems of different upper state vibrational quantum numbers, as shown in Fig. 12. T_v values determined from this method are shown in Fig. 11 as a function of distance from the model along the stagnation streamline.

An error analysis similar to that of T_r was performed to estimate the uncertainty in T_v. The estimated uncertainty in T_v because of the background signal σ_{T_v} is plotted as an error bar in Fig. 11. There is also an uncertainty contribution from the relative Franck–Condon factors of the spectral features. This has not yet been included in the uncertainty analysis.

In Fig. 11, the T_r values are higher than the T_v values at positions near the shock front and this trend continues up to the positions nearest the model. At the positions closest to the model, the T_r and T_v values agree within their uncertainties.

As shown in Fig. 7d, the emission from the shock layer contains two O-atom lines. The T_e of the shock layer was determined using the ratio of intensities from the two strong O-atom lines at 777 and 845 nm. As was derived in Ref. 5, T_e can be obtained from

$$T_e = \frac{(\theta_1 - \theta_2)}{\ell n(CI_2/I_1)} \tag{3}$$

where I, θ, and C represent the line intensity, characteristic temperature, and ratio of constant factors for the two transitions, respectively. In Fig. 13, the determined T_e values are

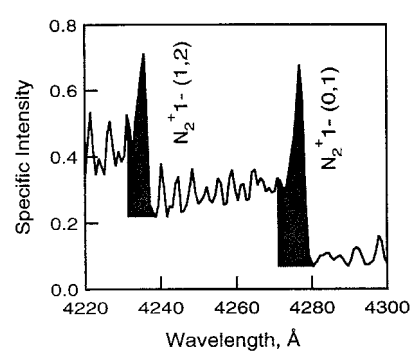

Fig. 12 Pair of areas that represent the integrated specific intensity used in the determination of vibrational temperature.

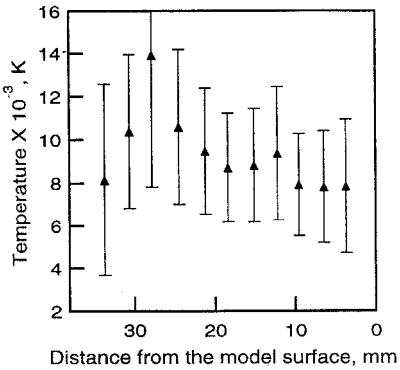

Fig. 13 Electronic temperature as a function of the distance from the model surface.

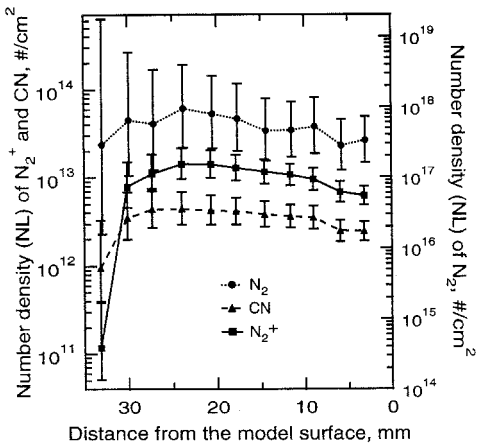

Fig. 14 Integrated number density distribution of N_2, N_2^1, and CN along the stagnation streamline. *N* and *L* represent the number density (#/cm^3) and optical path length along which the number density was integrated, respectively.

plotted as a function of distance from the model surface. Compared to Fig. 11, T_e is systematically higher than T_v throughout the shock layer. It is possible that this difference between T_e and T_v was caused by a strong signal contribution from the shock-front radiation, which may be in thermal nonequilibrium, to the total emission recorded along the LOS. Also, this discrepancy could be a result of a systematic error that occurs because the signals used in the ratio are measured at two different grating positions.[5] Although these grating positions are not widely separated in wavelength, there appears to be a discontinuity in the measured spectral response for these two positions. The uncertainties in the electronic temperatures were obtained from an analysis that included the uncertainties in Einstein coefficients and measured atomic line intensity.[5] The uncertainties are represented by the error bars in Fig. 13 and their magnitudes are quite large.

Number Density

Once the LOS-averaged temperatures were determined, they could be used to derive LOS-averaged species number densities by invoking an assumption that the electronic state populations follow a Boltzmann distribution.

For molecular species with known values of T_r, T_v, and T_e, correlations between the constituent number density and the spectral intensity can be generated using NEQAIR. Then, the absolute magnitudes of the measured spectra were used to determine the species number densities based on the correlations. In the current study, N_2^+ 1− (1, 0), N_2 2+ (0, 0), and CN violet (0, 0) bands in Figs. 7b and 7c were used to determine the number densities of N_2^+, N_2, and CN, respectively.

However, as seen in Figs. 7a–7d, there was no easily resolvable emission from different upper electronic states of a single molecular specie. Thus, T_e of the molecular species could not be directly determined from the obtained spectra. For this study, given the lack of a direct measurement of T_e for molecular species and the magnitude of the uncertainty in T_e obtained from the atomic oxygen, the molecular electronic states were assumed to be populated according to $T_v = T_e$.[9]

The number densities of N_2^+, N_2, and CN are plotted in Fig. 14. Therein, the values are given in units of cm^{-2}, which represents the number density integrated along the optical path. The uncertainty in number densities of molecular species is driven strongly by the uncertainty in T_e, which was assumed to be same as T_v, and, to a lesser extent, by the uncertainty in calibration of the absolute intensity. The total uncertainties in number density values were calculated by Eq. (1), where the σ were the standard deviations caused by the uncertainty in T_v. The estimated uncertainty is indicated by the magnitude of the error bars that are also shown in Fig. 14.

Discussion

LOS and Spatial Resolution

In emission measurements, the optical system collects photons from emitting gas particles in the light acceptance volume along the LOS direction as well as those from gas particles within the object area located at the optical focus. To understand how the present measurements were influenced by this effect, an optical ray analysis was performed. In Fig. 15, one of the eight light acceptance volumes is sketched with a coordinate system. Therein, the x and z axis represent the direction of stagnation streamline and LOS, respectively. The dimensions of the planar area of the acceptance volume, Δx and Δy, were then calculated using ray-tracing software.[10]

In Fig. 16, the calculated dimensions of the planar area are plotted as functions of the distance along the LOS direction, i.e., the z direction in Fig. 15. As Fig. 16 clearly shows, the actual dimensions of the rectangular area in the xy plane on the stagnation streamline are quite different from those of the theoretical calculation presented in Fig. 3. This was caused by astigmatism, which originated from the tilting of the spherical

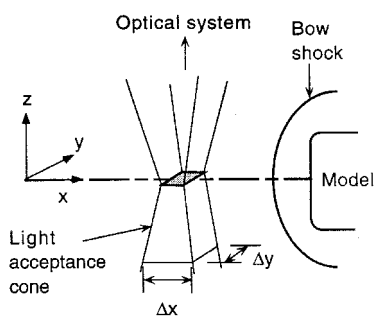

Fig. 15 Schematic of the light collecting cone.

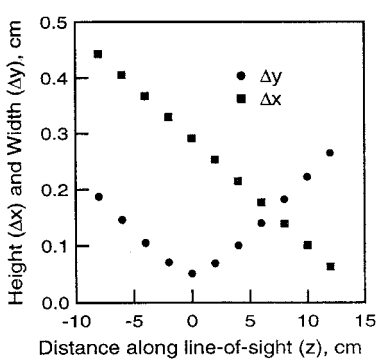

Fig. 16 Dimension of the cone in Fig. 15 as functions of the distance along the LOS direction. The coordinate system was indicated in Fig. 15.

focusing mirror. The off-axis angle, denoted by α in Fig. 2, of the focusing mirror was 11 deg.

The axial dimension of the light acceptance volume for the optical configuration used in this study was not small compared to the shock-layer thickness. This attribute of the light collection geometry causes an averaging of the axial flow gradients, because the measurement locations partially overlap near the shock front region.

As the experimental data were acquired at only one set of spanwise locations along the stagnation streamline, there was not sufficient information to perform an Abel transformation. Consequently, only properties of the nonuniform flow that were spatially averaged along the optical path could be determined from this experimental data. Thus, instead of mapping out the flow properties point-by-point for comparison with computations, comparisons were limited to spatially averaged quantities and emission spectra that were calculated using NEQAIR with flow properties from a numerical solution. In Ref. 11, more detailed analyses based on these comparisons were performed to determine the flow characteristics.

Temperatures

All temperatures in the previous sections were determined based on the emission spectra that carry the information of excited electronic states. Thus, the obtained temperatures represent the population distribution of the excited electronic states. For the temperature range in Figs. 11 and 13, the population in electronically excited states was quite small compared to that of the ground states for all species. Consequently, the thermal status of the excited states may not represent that of the total flow and this should be kept in mind during subsequent discussions.

As NO γ and δ bands systems have different upper electronic states, the electronic temperature of the freestream could be determined from the spectra in Fig. 5. Based on the peak ratio of NO γ and δ bands, the determined value was 12,950 $\pm$ 800 K, assuming a Boltzmann distribution among the electronic states of NO. For this measurement 1) the assumption of the Boltzmann distribution was probably not satisfied because the other NO systems did not appear in the spectra, and 2) the exact mechanism of the electronic excitation for NO under the conditions of current study was not known.

Small errors in the ratios used in current study can cause large errors in temperatures. The background errors caused by the stray light can be reduced by using a higher quality spectrograph and a holographic grating. Also, the solid angle of the light-acceptance volume can be decreased by further limiting the aperture of the imaging spherical mirror. These will be explored in future study.

As shown in Figs. 11 and 13, all of the temperatures overlap within their error bounds at two locations near the model surface. It may indicate that the thermal equilibrium was reached near the model surface. More detailed analysis on the relaxation and equilibration process is reported in Ref. 11.

Number Densities

In Fig. 14, LOS-integrated number density values were presented for N_2^+, N_2, and CN for the measurement locations in the shock layer. Inside of the shock-front region, all of the distributions showed relatively small variations in the axial distribution. Actual species number densities may be varying considerably in this region, but the path-integrated nature of the measurement obscures this variation. This makes it impractical to infer the chemical status of the flow from these measurements. In addition, because of the decreased spatial resolution effect described earlier in this section, measured axial property gradients will tend to be smoothed.

Summary

Spectroscopic measurements were conducted in the 20-MW AHF at Ames Research Center using a CCD camera capable of recording radiation at eight locations along the stagnation streamline. Emission spectra from the freestream and shock-layer flow around a model were taken for the investigation of flow characteristics. Spectral features were used to identify the species present in the flow.

LOS-averaged values of T_r for the freestream, and T_r, T_v, and T_e in the shock layer, were determined. For the shock-layer flow all temperature values agreed within their uncertainties at the two positions closest to the model. This may indicate a region of thermal equilibrium near the model at the test conditions. Optical-path-integrated species number densities were determined using the temperatures and the absolute intensities of their respective emission features. However, no determination of the chemical state of the flow could be made from the experimental data alone.

Detailed comparisons between calculated spectra based on the numerical simulation and the experimentally measured spectra have been performed and are reported in Ref. 11.

Acknowledgments

The authors acknowledge the support of the Reacting Flow Environments Branch at NASA Ames Research Center through Contract NAS2-14031 to Eloret. Special thanks are given to Ellis Whiting for this advice. Support of STM, STF, and AHF personnel are also greatly appreciated.

References

[1]Watson, V. R., and Pegot, E. B., "Numerical Calculations for the Characteristics of a Gas Flowing Axially Through a Constricted Arc," NASA TN D-4022, June 1967.

[2]Sharma, S. P., Park, C. S., Newfield, M. E., Balboni, J., Scott, C. D., Arapelli, S., and Taunk, J., "Arcjet Flow Characterization," AIAA Paper 96-0612, Jan. 1996.

[3]Park, C., "Experimental Evaluation of Real-Gas Phenomena in High-Enthalpy Aerothermal Test Facilities," AIAA Paper 96-2207, June 1996.

[4]Babikian, D. S., Park, C., and Raiche, G. A., "Spectroscopic Determination of Enthalpy in an Arc-Jet Wind Tunnel," AIAA Paper 95-0712, Jan. 1995.

[5]Park, C. S., Newfield, M. E., Fletcher, D. G., Gökçen, T., and Sharma, S. P., "Spectroscopic Emission Measurements Within the Blunt-Body Shock Layer in an Arc-Jet Flow," AIAA Paper 97-0990, Jan. 1997.

[6]Park, C., "Nonequilibrium Air Radiation (NEQAIR) Program: User's Manual," NASA TM 86707, July 1985.

[7]Laux, C. O., "Optical Diagnostics and Radiative Emission of Air Plasmas," Ph.D. Dissertation, Stanford Univ., Stanford, CA, 1993.

[8]Kline, S. J., and McClintock, F. A., "Uncertainties in Single-Sample Experiments," *Mechanical Engineering*, Vol. 75, No. 1, 1953, pp. 3–8.

[9]Park, C., "Assessment of a Two-Temperature Kinetic Model for Dissociating and Weakly Ionizing Nitrogen," *Journal of Thermophysics and Heat Transfer*, Vol. 2, No. 1, 1988, pp. 8–16.

[10]"Beam 3 Optical Ray Tracer," Stellar Software, Berkeley, CA.

[11]Gökçen, T., Park, C. S., Newfield, M. E., and Fletcher, D. G., "Computational Simulation of Emission Spectra from Shock Layer Flows in an Arc-Jet Facility," AIAA Paper 97-0135, Jan. 1997.